ASTFE American Society of Thermal and Fluids Engineers

Proceedings of the 2nd Thermal and Fluid Engineering Conference, TFEC2017
4th International Workshop on Heat Transfer, IWHT2017
April 2-5, 2017, Las Vegas, NV, USA

TFEC-IWHT2017-xxxxx

LARGE EDDY SIMULATIONS OF ARGON BUBBLE TRANSPORT AND CAPTURE IN MOLD REGION OF A CONTINUOUS STEEL CASTER

Kai Jin[1], Surya P. Vanka[1*], Brian G. Thomas[1,2]

[1]University of Illinois at Urbana Champaign, Urbana, IL 61801, USA
[2]Colorado School of Mines, Golden, CO 80401, USA

ABSTRACT

More than 90% of steel produced globally every year is made using the continuous casting process. In this process, argon gas is usually injected to prevent nozzle clogging. The gas bubbles affect the flow pattern through the bubble drag, and may become entrapped to form defects in the final product. To investigate this problem, we have developed and applied a two-way coupled Eulerian-Lagrangian computational model with Large Eddy Simulations of the turbulent flow and transport and capture of argon bubbles by the solidifying shell. A practical steel caster is considered, and the domain is discretized with more than 16 million hexahedra finite volume cells. The turbulent flow is computed using the Large Eddy Simulation (LES) approach. The trajectories of 1.2 million argon bubbles were tracked by solving the transport equations for each individual bubble. A previously validated particle capture criterion is used to predict the capture of the argon bubbles. The equations are solved on a graphic processing unit (GPU) using an in-house code CUFLOW. The results show that less bubbles are captured in the current LES model when compared with a RANS model. The captured bubble sizes and numbers agree well with plant measurements.

KEY WORDS: Continuous casting of steel, Large Eddy Simulation, Argon bubble transport, Bubble capture

1. INTRODUCTION

In continuous casting of steel, argon gas is usually injected to prevent nozzle clogging. [1–3] However, argon bubbles also affect the flow pattern, and may become entrapped to form defects, such as blisters and slivers, in the rolled steel product. [4,5] After entering the Submerged Entry Nozzle (SEN), argon bubbles are carried by the turbulent flow through the SEN into the mold cavity region, where they greatly affect the flow pattern, surface level fluctuations, and slag entrainment. Bubbles entering the mold region may end up at three locations: (1) most large bubbles reach the top surface, pass through the slag layer and escape harmlessly to the atmosphere;[6,7] (2) some are captured near the meniscus and lead to surface defects; (3) some of the small bubbles are captured deep in the caster and cause internal defects. During the transport, moving bubbles can also collect non-wetting inclusion particles, such as alumina. If bubbles are captured into the cast steel product, the layer of inclusions covering the bubble surface will lead to oxide clusters, and severe sliver defects.[8,9]

Computational models and water models have been used to study the two-phase flow of argon and molten steel in the SEN and mold region of continuous casters. [6–25] Both Eulerian-Eulerian [11,19–21,26] and Eulerian-Lagrangian [10–16,18,27] approaches have been used in computational models. Because of high gas fractions, two-way coupled models are more appropriate as the argon gas affects the steel flow and vice versa. [10–12,22] Increasing Ar gas causes increased upward flow near the SEN and tends to revert the classic double-roll flow pattern to a single-roll pattern with the surface flow moving away from the SEN towards the narrow face. [11,20,21]. Asymmetric, oscillating flow is observed if gas fractions are excessive

*Corresponding Author: spvanka@illinois.edu

[1,28]. Argon bubbles in steel are reported to be larger than air bubbles in water [22,29], and increasing the gas flow generates more and larger bubbles. [1,28,29] Recently, the MUSIG model [30] has been used to model this multi-phase flow problem using an Eulerian-Eulerian approach to include the effect of local bubble size. [22,31]

Several studies [12,14–18,23,25,32–34] have investigated the capture fraction and distribution of inclusion particles in continuous casting, but none of these studies have included the coupled effects of Ar gas on the flow field. Recent studies [6,7] used the Reynold-averaged Navier Stokes (RANS) model with a Lagrangian approach to investigate the transport and capture of argon bubbles. The turbulent dispersion of individual particles was represented by a Random Walk Method. [12,13,16–18,22–25,27,32,33] This approach includes the effect of bubbles with different diameters on the local fluid flow. By tracking the motion of each individual bubble and using an advanced capture criterion [15,16,24], it was found that ~85% of small (< 0.08 mm) bubbles are captured. However, only a very small fraction of large bubbles is captured (< 0.02%). The predicted capture location and size of bubbles matched with plant experiments in most places except in the region very close to the meniscus, where the capture rate is under predicted by the model. This may be due to absence of a mechanism of bubble capture by hooks. [5]

In this paper we investigate the transport and capture of argon bubbles using a LES model for the turbulent steel flow and a Lagrangian description of the motion of the argon bubbles. This study more realistically represents the instantaneous turbulent flow and the transport of the bubbles / particles with the instantaneous flow without using the random walk assumption for turbulent fluctuations.

2. COMPUTATIONAL MODELS AND NUMERICAL METHODS

A three-dimensional finite-volume computational model together with a two-way coupled Lagrangian particle tracking method was applied to study the fully-coupled turbulent flow and transport of argon bubbles in a commercial continuous steel caster. The computational domain included the slide gate, SEN and mold region (from meniscus surface to 2.65 m below meniscus), as shown in Fig. 1. In the plant operation, 1300 mm wide slabs were cast at 1.5 m/min with the slide gate open at 70% [6,7], as illustrated in Fig. 1.

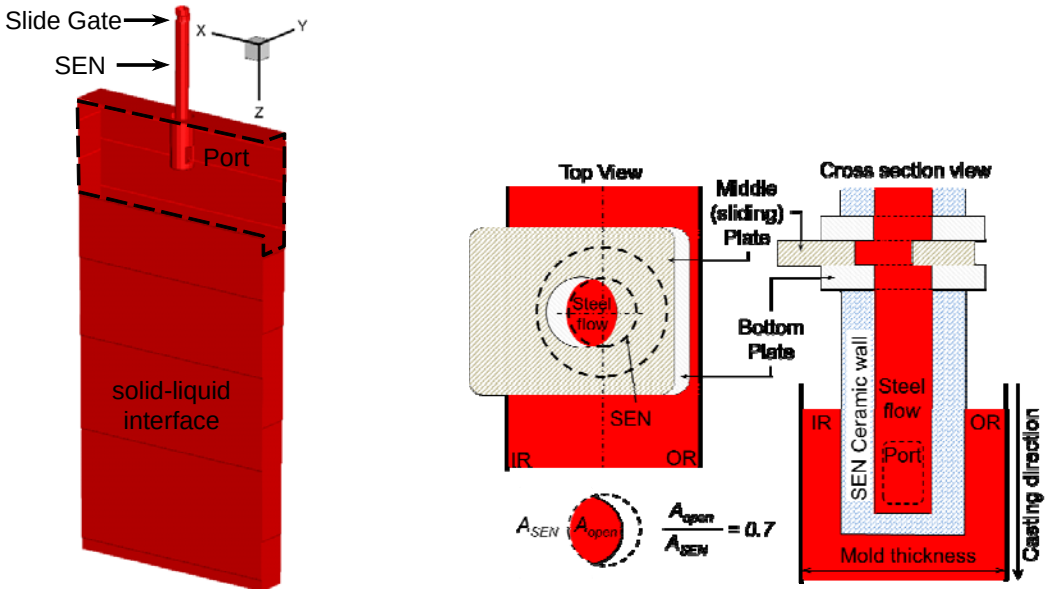

Fig. 1 Computational domain including slide gate, SEN, mold region and solid shell.

The computational domain was discretized using ~16 million hexahedral finite volume cells. Casting conditions were taken as described in the references [6,7] and listed in Table 1. The assumed shell thickness s (mm) at any point z (m) below the meniscus is calculated as

$$s = k\sqrt{z / V_c} \tag{1}$$

where V_c = 0.025 m/s (1.5 m/min) denotes the casting speed and the constant k = 3 mm/s^{½} is chosen to match a break-out shell profile from the caster at Baosteel.

Table 1. Process parameters

Process Parameters	Value
Mold thickness (L_t)	230 mm
Mold width (L_w)	1300 mm
SEN Submergence depth	160 mm
Nozzle port downward angle	15°
Nozzle port area (width × height)	65×83 mm^2
Casting speed (V_c)	1.5 m/min
Argon volume fraction (α)	8.2 vol%
Steel density (ρ)	7000 kg/m^3
Argon density (ρ_p)	0.5 kg/m^3
Steel viscosity (μ)	0.0063 kg/(m·s)
Ar viscosity (μ_p)	0.0000212 kg/(m·s)

2.1 Governing Equations for the Steel Flow

In this work the turbulent flow in the SEN and mold is simulated by the LES approach. The three-dimensional time-dependent Navier Stokes equations given below were solved:

$$\nabla\cdot\left(\rho\boldsymbol{u}\right) = \dot{s} \tag{2}$$

$$\rho\frac{\partial\boldsymbol{u}}{\partial t} + \rho\left(\boldsymbol{u}\cdot\nabla\right)\boldsymbol{u} = -\nabla p + \nabla\cdot\left[\left(\mu+\mu_{sgs}\right)\left(\nabla\boldsymbol{u}+\nabla\boldsymbol{u}^T\right)\right] + \boldsymbol{S}_{\text{sink}} + \boldsymbol{S}_p \tag{3}$$

where ρ is the density of molten steel, $\dot{s}$ and $\boldsymbol{S}_{\text{sink}}$ are the mass and momentum sink terms [7,15,35] added to include the effect of the solidifying shell, $\boldsymbol{u}$ is the velocity vector, p is a modified static pressure which includes the normal stresses, $\boldsymbol{S}_{\text{p}}$ is the source term due to two-way coupled Lagrangian particle tracking, μ is the dynamic viscosity of the molten steel and μ_{sgs} is the eddy viscosity that represents the subgrid stress. In this study, μ_{sgs} is modeled by the coherent-structure Smagorinsky model (CSM) sub-grid scale (SGS) model [36]. In the CSM SGS model, μ_{sgs} is computed as:

$$\mu_{sgs} = \rho\nu_{sgs} = \rho\left(C_s\Delta\right)^2\sqrt{2\|\mathbf{S}\|^2} \tag{4}$$

where Δ is the size of the cubic cell and $\mathbf{S}$ is the rate-of-strain tensor given by $\boldsymbol{S} = (\nabla\boldsymbol{u}+\nabla\boldsymbol{u}^{\text{T}})/2$. C_{s}^2 is calculated locally by the following equations:

$$C_s^{\,2} = C_{CSM}\left|\frac{Q}{E}\right|^{3/2}\left(1-\frac{Q}{E}\right) \tag{5}$$

$$Q = \frac{1}{2}\left(\|\mathbf{W}\|^2 - \|\mathbf{S}\|^2\right) \qquad E = \frac{1}{2}\left(\|\mathbf{W}\|^2 + \|\mathbf{S}\|^2\right) \tag{6}$$

where C_{csm} = 1/22 is a model constant and $\boldsymbol{W} = (\nabla \boldsymbol{u} - \nabla \boldsymbol{u}^{T})/2$ is the vorticity tensor. The CSM model appropriately damps the eddy viscosity in the wall boundary layer regions and also automatically incorporates the effect of anisotropy induced by the applied magnetic fields on the subgrid scales [37]. Therefore, no additional modifications to account for anisotropic subgrid effects are needed or added. This model has been successfully tested and used previously in predicting fluid flow in steel casters with magnetic fields [38,39].

2.2 Two-way Coupled Lagrangian Model for Argon Bubbles

In plant operation, Argon gas is injected through a porous refractory in the upper tundish nozzle and SEN to prevent nozzle clogging. In this work, the argon gas volume was distributed into bubbles according to a Rosin-Rammler [40] size distribution with average bubble diameter d_{mean} = 3 mm and spread parameter η was taken as 4. These are the same parameters used in previous RANS simulations. [6,7] These two parameters are chosen based on calculations with a previously-validated two-stage model of Ar injection into downward flowing steel [1,29] and adjusted to account for increased surface tension in steel/argon using a relation from previous measurements [1,29] and recent measurements[41] of bubble distributions. In the simulation, 407 bubbles were randomly placed slightly below the slide gate every 0.01 second. The number distribution of bubbles is shown in Fig. 2. For a 30 second LES simulation, the trajectory of 1.2 million bubbles are tracked by solving the equations of motion for each individual particle:

$$\frac{\mathrm{d}\boldsymbol{x}_p}{\mathrm{d}t} = \boldsymbol{u}_p \tag{7}$$

$$m_p \frac{\mathrm{d}\boldsymbol{u}_p}{\mathrm{d}t} = \boldsymbol{F}_{pT} = \sum \left(\boldsymbol{F}_{pD} + \boldsymbol{F}_{pL} + \boldsymbol{F}_{pP} + \boldsymbol{F}_{pA} + \boldsymbol{F}_{pB} \right) \tag{8}$$

where $\boldsymbol{u}_p$ and $\boldsymbol{x}_p$ are the particle velocity vector and position vector, respectively. The total force, $\boldsymbol{F}_{pT}$, acting on an individual bubble is the sum of five forces: drag force $\boldsymbol{F}_{pD}$, lift force $\boldsymbol{F}_{pL}$, added mass force $\boldsymbol{F}_{pA}$, pressure gradient force $\boldsymbol{F}_{pP}$ and buoyancy/gravity force $\boldsymbol{F}_{pB}$. Note that the motion of each bubble is not dependent of other bubbles, thus the particle trajectory calculations are independent and ideal for parallel processing.

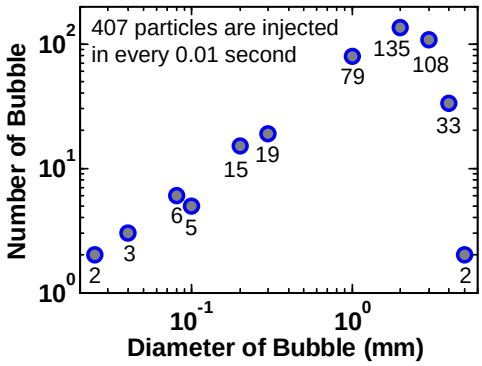

Fig. 2 Number distribution of the 407 bubbles injected into the domain every 0.01 second

Forces on argon bubbles. The drag force acting on a single bubble is calculated as:

$$\boldsymbol{F}_{pD} = \frac{C_D}{24} \frac{18\mu}{d_p^2} V_p \left(\boldsymbol{u}_{Fp} - \boldsymbol{u}_p \right) Re_p \tag{9}$$

where V_p is particle volume, Re_p is particle Reynolds number, $\boldsymbol{u}_{Fp}$ is the fluid velocity at particle location, and C_D is the drag coefficient. Unlike solid particles, argon bubbles deform during transport in the turbulent flow. The deformation of bubbles causes variation in the drag force. In this study, the drag coefficient relation proposed by Kuo *et al*. [42] is used, and the drag coefficient is computed based on bubble Reynolds number and Weber number *We* as follows:

$$C_D = \begin{cases} 16Re_p^{-1} & Re_p \le 0.49 \\ 20.68Re_p^{-0.643} & 0.49 < Re_p \le 100 \\ 6.3Re_p^{-0.385} & 100 < Re_p \\ We/3 & 100 < Re_p \text{ and } Re_p > 2065.1We^{-2.6} \\ 8/3 & 100 < Re_p \text{ and } We > 8 \end{cases} \tag{10}$$

where $We = \dfrac{\rho_l d \left|\boldsymbol{u} - \boldsymbol{u}_p\right|^2}{\gamma_{lg}}$ and γ_{lg} = 1.2 N/m is the surface tension between argon and steel. This model takes into account the bubble shape. The lift force, pressure gradient force, added mass force and buoyancy force are computed as follows:

$$\boldsymbol{F}_{pL} = C_L \rho V_p \left(\boldsymbol{u}_p - \boldsymbol{u}_{Fp}\right) \times \left(\nabla \times \boldsymbol{u}_{Fp}\right) \tag{11}$$

$$\boldsymbol{F}_{pP} = \rho V_p \frac{\mathrm{D}\boldsymbol{u}_{Fp}}{\mathrm{D}t} \tag{12}$$

$$\boldsymbol{F}_{pA} = 0.5 C_V \rho V_p \left(\frac{\mathrm{D}\boldsymbol{u}_{Fp}}{\mathrm{D}t} - \frac{\mathrm{d}\boldsymbol{u}_p}{\mathrm{d}t} \right) \tag{13}$$

$$\boldsymbol{F}_{pB} = \boldsymbol{g} V_p \left(\rho_p - \rho\right) \tag{14}$$

where C_L and C_V are the lift and added mass coefficients, respectively. In this study, C_V is taking as 1.0 [43], and C_L is calculated using the Legendre and Magnaudet lift force model [44]. The motion of argon bubbles can affect the fluid flow through the source term ($\boldsymbol{S}_p$) in the momentum equation:

$$\boldsymbol{S}_p = \sum_{i=1}^{n} \boldsymbol{S}_{p,i} = -V_{\text{cell}}^{-1} \sum_{i=1}^{n} \left(\boldsymbol{F}_{pD} + \boldsymbol{F}_{pL} + \boldsymbol{F}_{pA} + \boldsymbol{F}_{pP} \right) \tag{15}$$

where V_{cell} is the cell volume and n is the number of the particles contained in the finite volume.

Effect of SGS on argon bubble dispersion. The dispersion of bubbles by the SGS motion is included by adding a SGS velocity to the fluid velocity at the particle location. In this approach, the SGS kinetic energy k_{sgs} is computed from the turbulent subgrid viscosity using the Yoshizawa SGS model [45]

$$\nu_{sgs} = 0.066 \Delta k_{sgs}^{1/2} \tag{16}$$

When evaluating the forces exerted on particles using equations (6) – (11), the resolved fluid velocity at particle location, $\overline{\boldsymbol{u}}_{Fp}$, is first obtained from interpolation using Lagrange polynomials. Then a random fluctuation velocity $\boldsymbol{u}_{sgs}$ is added to $\overline{\boldsymbol{u}}_{Fp}$ to compute $\boldsymbol{u}_{Fp}$

$$\boldsymbol{u}_{Fp} = \overline{\boldsymbol{u}}_{Fp} + \boldsymbol{u}_{sgs} \tag{17}$$

$$\boldsymbol{u}_{sgs} = \boldsymbol{\zeta}\sqrt{\frac{2k_{sgs}}{3}} \tag{18}$$

where $\boldsymbol{\zeta}$ is a random vector with components having a standard normal distribution with zero mean and unity standard deviation.

Capture Criterion. Different criterion can be used to predict the capture of argon bubbles. The simplest criterion assumes that argon bubbles are captured when they touch the solidification front. This criterion shows satisfactory results if the argon bubbles are small (hundreds of microns), but it may over-predict the capture of large bubbles or inclusions. [7] In the present work, an "advanced" capture criterion based on force balance is implemented. This criterion assumes that small bubbles less than the Primary Dendrite Arm Spacing (PDAS) can enter between the dendrite arms and be captured by entrapment. For bubbles/particles greater than the PDAS, the advanced criterion considers eight forces acting on a spherical bubble/particle touching the dendrite arms. [15,16,24]

2.3 The Solver

The above governing equations are solved with an in-house code CUFLOW [46–49] which utilizes Graphics Processing Units (GPU) for the arithmetic computations. The code was written using CUDA Fortran, and has been extended to be able to work on multiple GPUs in parallel through the Message Passing Interface (MPI) [49]. In CUFLOW, a fractional step method is used to solve the continuity and momentum equations. Pressure and electric potential Poisson equations are solved efficiently by a V-cycle multigrid method, and red-black Successive Over Relaxation (SOR) on GPUs with over-relaxation parameter of 1.6. Details of the solution algorithm are available in references [47–49]. The particle transport equations are parallelized onto GPUs and solved with high efficiency. CUFLOW has been previously validated and applied to study the effect of magnetic field in a lid-driven cavity [50], argon bubble rise in liquid steel under a magnetic field [51], and the flow in the mold region of continuous casters of steel with and without EMBr [39,52].

3. RESULTS AND DISCUSSION

3.1 Motion of Liquid Steel

The flow pattern of molten steel in the mold region is critical to the final quality of product. Fig. 3 shows the time-averaged flow pattern in the symmetry plane of SEN, center plane of the mold one cm below the top surface. The liquid steel first enters the inner radius side of the SEN with a maximum speed of ~3 m/s, forms a recirculation region of length ~0.2 m on the outer radius side beneath the middle of the sliding plate. Two equal-sized swirls are seen at the SEN bottom. The stream traces in the center plane (y = 0) show a typical double role flow pattern. Near the top surface, the fluid moves almost parallel to the wide face with a speed of 0.25 to 0.3 m/s without any cross flow. This flow pattern predicted by LES is seen to be different from that predicted using the RANS approach. [7] In the previous RANS simulation, the top region of each half mold contains two big eddies: one beside the SEN and the other close to the narrow face. The eddy beside the SEN was driven by the buoyancy of the argon gas. The eddy close to the narrow face was caused by the jets impinging and splitting on the narrow face, sending partial flow upwards and across the top surface toward the SEN. [7] The eddy beside the SEN disappears in the transient LES simulation, owing to the buoyancy of the rising argon gas. In the previous RANS simulations, most argon bubbles followed the time-averaged flow pattern which caused concentrated momentum only in cells that are near the SEN. However, in LES the time dependent behavior of the swirls at the bottom of SEN is resolved. The swirls inside the port frequently switch directions, and the unsteady swirling jet sends argon bubbles to different locations at different times. The RANS model predicted that the swirl in the nozzle was from inner to outer radius, which results in more bubbles exiting the port near the inner radius. The floatation of those bubbles forms the eddy close to the nozzle.

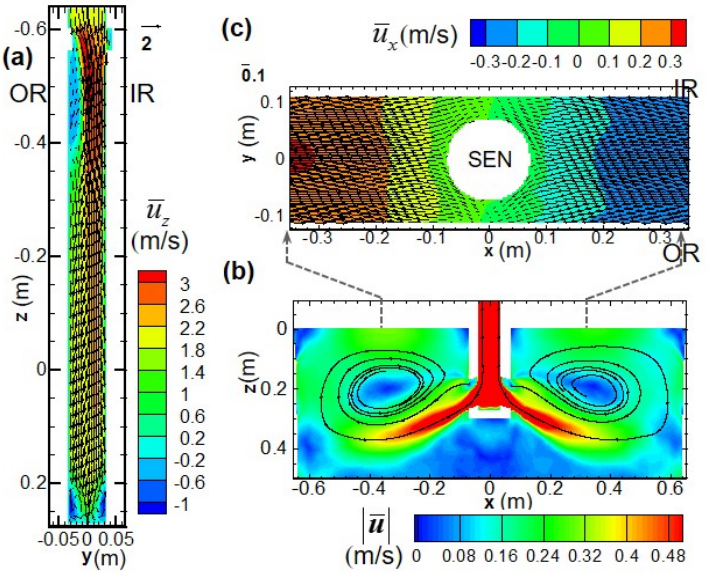

Fig. 3 Predicted flow patterns in the (a) symmetry plane of SEN, with velocity vectors and contours of z-velocity; (b) center plane of the mold with contours of velocity magnitude; (c) 1 cm below the meniscus region with contours of x-velocity components.

3.2 Transport of Argon Bubbles

Figure 4 shows contours of steel velocity and position of bubbles (within 2 mm in/out of the symmetry plane) in the symmetry plan of SEN (x = 0) at time t = 24 s. Bubbles are randomly injected in a cylindrical shape region below the slide gate with zero initial velocity. Most bubbles are carried downward by the high velocity steel flow.

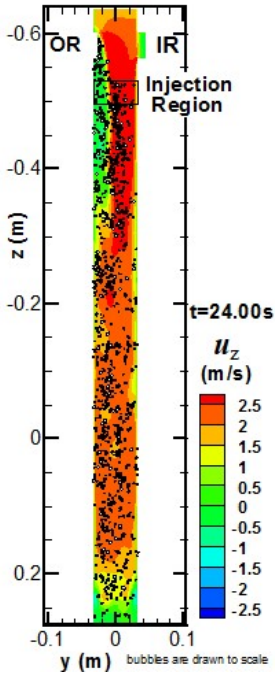

Fig. 4 Contours of z-velocity in the symmetry plane of SEN (x = 0). Argon bubbles with centers located within the region: -2 mm < x_p < 2 mm are shown.

In the recirculation region below the slide gate, many bubbles move up into the slide gate and accumulate below the middle of the sliding plate which implies a form of gas pocket, as also observed in a water model experiment. Since much of the region in the mold has only a low argon gas volume fraction we did not include any collision or coalescence model. Therefore, our study does not directly predict formation or shape of the gas pocket. To predict such gas pockets, a Eulerian-Eulerian formulation is needed, which is beyond the scope of the presented work. No bubbles are seen in the upper slide gate as the downward moving steel flow carries the bubbles downward.

Fig. 5 shows contours of *x*-direction velocity in the center plane and positions of argon bubbles that are within 2 mm to the middle plane (-2 mm < y_p < 2 mm) at t = 24 seconds. Most bubbles that enter the mold region with a high velocity of 1.2-1.5 m/s follow a thin layer of jet which is around 3 cm thick. Near the top backflow region of the port, some argon bubbles travel opposite to the port. Above the jet at an outside port, an eddy is shed carrying some large bubbles with it. This vortex shedding is a result of Kelvin–Helmholtz instability at the jet boundary and buoyancy force by a group of bubbles that tear the jet and intensify the instability. Close to the SEN, the path lines indicate that buoyancy due to bubbles drives the flow upwards, then it meets the downward going flow and forms small eddies in the upper portion of the mold. Near the top surface, most bubbles rise towards the SEN side. However, some small bubbles move downward with the steel flow.

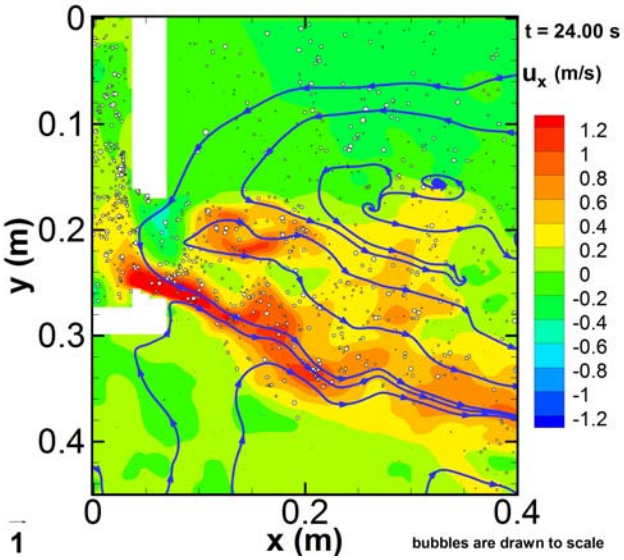

Fig. 5 Contours of *x*-velocity and positions of bubbles in the middle plane (y = 0 mm) at 24 second The (bubbles with centers in the region: -2 mm < y_p < 2 mm). Stream traces indicate the motion of the molten steel flow.

3.3 Capture and Removal Rate of Argon Bubbles

During the simulation, bubbles are continually injected into the domain with an injection rate of 40,700 bubbles per second. After a few seconds, a large number of big bubbles escape from the top surface and some small bubbles are captured by the solid shell. In Fig. 6, the black line shows the accumulation of argon bubbles inside the caster. It starts with zero and increases linearly in the beginning of the simulation because bubbles have not reached the top surface or being captured yet. After 30 seconds the total number of bubbles inside the domain reaches 2.2×10^5 and increases very slowly due to it reaching a quasi-steady state where rate of bubbles escaping and being captured roughly equals the injection rate. The triangle symbols show that the bubble escape rate from top surface is roughly equal to the injection rate of 40,700 particles per second. The rate of bubbles captured by the shell is approximately 400 to 600 bubbles per second which is 100 times smaller than the injection rate, indicating an overall capture fraction around one percent.

Fig. 7 shows the total number of bubbles injected and the number that remain in the domain (at t = 32 seconds) as a function of bubble size. After 32 seconds, the number distribution of the bubbles that remain inside the domain is different compared with the distribution of injected bubbles. For small bubbles ($d_p \leq 0.3$ mm) the number of bubbles remaining inside the domain is almost proportional to the number of bubbles of same size originally injected into to the domain. However, for larger bubbles, the number of large bubbles remaining in the caster is much less than the number injected, because of the large escape rate of the large bubbles. The percentile numbers in the figure show fractions of bubbles remaining in the caster. The fractions of large bubbles remaining are small (4 to 22%.) as most escape. For bubbles of $d_p \leq 0.1$ mm the fractions are ~68 pct. as many of them are captured by the shell. A maximum fraction of ~77% is seen for bubbles between 0.1 and 0.2 mm diameter, as the buoyancy forces on these bubbles are not large enough to easily bring them to the top surface, while they are also more difficult to be captured by the solidifying shell compared to the very small bubbles.

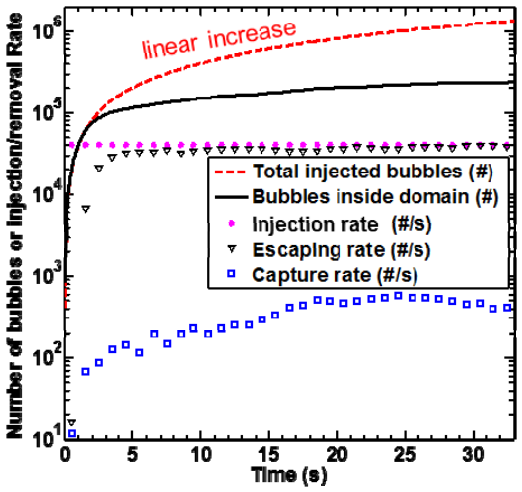

Fig. 6 Number of injected particles, number of bubbles still remains moving inside the cater, injection rate, removal rate (particles escaped from top surface) and capture rate (captured by shells) at different time.

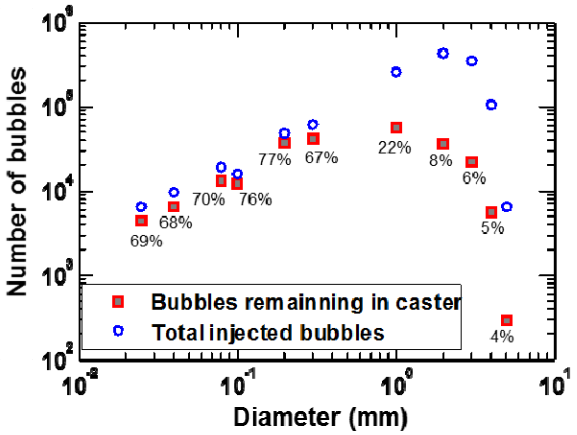

Fig. 7 Number of bubbles remaining in the domain for different bubble sizes (t = 32 second). The percentage numbers show the ratio of number of bubbles still moving inside the caster to the number of total injected bubbles.

3.4 Comparisons of LES Model with Previous RANS Model and Plant Measurements

Previously Jin et al. [6,7] used RANS with a random walk model and two particle capture criteria to study the transport and capture of argon bubbles under the same casting conditions as in this study. In addition, a step milling experiment was carried out in the plant to investigate the size of the captured argon bubbles. Fig. 8 shows the predicted average bubble diameter beneath the strand narrow face surface. These experimental results are compared below with RANS predictions and LES. [6,7] The star symbols show the results of RANS random walk model with simple capture criterion which assumes that bubbles are captured upon touching the surface.

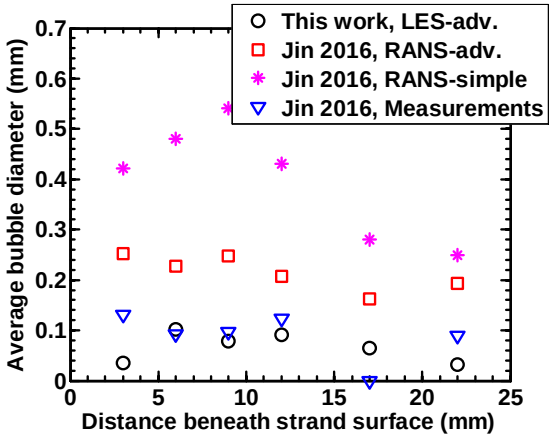

Fig. 8 Comparison of predicted average bubble diameter on narrow face with previous RANS model and plant measurement.

This assumption greatly over-predicts the average bubble diameter. After using the advanced capture criterion [15,16,18] the results are seeing to improve, but still a larger average bubble diameter is predicted. This may be due to the over-prediction of capture of small bubbles ($0.2 \leq d_p \leq 0.3$ mm) as mentioned earlier. However, with the transient LES model, the predicted average bubble diameter is closer to that measured at Baosteel. [6,7] Similar results are seen for the wide face inner radius. Fig, 9 shows the average diameter of bubbles obtained from a sample

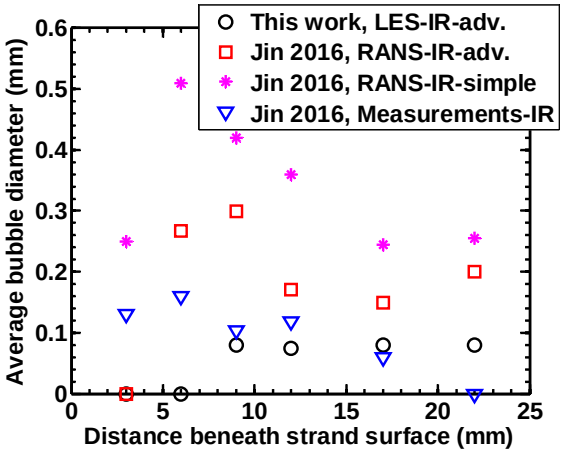

Fig. 9 Comparisons of predicted average bubble diameter on wide face (inner radius side) with previous RANS model and plant measurement.

cut from the center region (center of the wide face inner radius). The LES predicted that the average bubble diameter is also ~0.1 mm which matches well with measurements. However, both models predicted that no bubbles are captured in a region very close to the top strand. One possible reason is that currently hooks are not included, but hooks can capture the bubbles closer to the meniscus region. [5]

4. CONCLUSIONS

A multi-GPU-based LES code CUFLOW is applied to study the two-phase steel flow and capture of argon bubbles inside a commercial steel caster. The effect of sub-grid turbulent scales on bubbles dispersion is modelled. An advanced force balance capture criterion [15,16,18] was used to predict the capture of argon bubbles by the steel shell. Important findings of this work are summarized below:

1. With a casting speed of 1.5 m/min and 8% of argon gas injection rate, a double roll pattern is seen when the EMBr is turned off. The buoyancy force exerted on the argon bubbles is not strong enough to cause reverse flow (from SEN to NF) on top surface. This flow pattern is different from that observed in a previous study with the RANS approach.

2. The previous RANS study predicted that most large bubbles escaped very close to the SEN (< 0.3 m away from SEN center), while the current LES shows that the transient turbulent jets can send larger bubbles further away from the SEN center. This greater transport of argon bubbles reduces the flotation effect of the bubbles near the SEN region, thus no reverse flow is seen. The disagreement in the mean flow pattern predicted by the two approaches may also be due to the finite integration time of the LES simulation.

3. The Lagrangian bubble transport approach predicts that the bubbles accumulate in the back flow region beneath the slide gate and on top of the ports, which agrees with water model experiments. Accumulation of argon bubbles are also seen in the low pressure region of vortex center at the bottom of the SEN.

4. The LES model predicts that a smaller number of bubbles are captured in comparison with the RANS approach and the random walk model [2], especially for $0.2 \leq d_p \leq 0.3$ mm bubbles. The capture fraction is observed to be only 1 percent which is much less than that predicted by previous RANS simulation (~60 pct). The causes for this discrepancy may be the differences in the flow pattern predicted by the two models and the use of random walk in the RANS model which over-predicts the probability of the bubbles hitting the walls.

ACKNOWLEDGMENT

The authors thank the financial support from the National Science Foundation (Grant No. CMMI 11-30882) and the Continuous Casting Consortium, University of Illinois at Urbana-Champaign, USA. They thank Baosteel, Shanghai, P.R. China for providing the casting conditions and measurements. This research is also part of the Blue Waters sustained petascale computing project, which is supported by the National Science Foundation (awards OCI-0725070 and ACI-1238993) and the State of Illinois. Blue Waters is a joint effort of the University of Illinois at Urbana-Champaign and its National Center for Supercomputing Applications. The authors also thank NVIDIA Hardware Grant Program for providing the GPUs for an in-house workstation.

REFERENCES

[1] Bai, H., and Thomas, B. G., "Turbulent flow of liquid steel and argon bubbles in slide-gate tundish nozzles: Part I. Model development and validation," *Metall. Mater. Trans. B*, 32(2), pp. 253–267, (2001)

[2] Bai, H., and Thomas, B. G., "Effects of clogging, argon injection, and continuous casting conditions on flow and air aspiration in submerged entry nozzles," *Metall. Mater. Trans. B*, 32(4), pp. 707–722, (2001)

[3] Rackers, K. G., and Thomas, B. G., "Clogging in Continuous Casting Nozzles," *78th Steelmaking Conference Proceedings*, Iron and Steel Society, Nashville, TN, pp. 723–734, (1995)

[4] Knoepke, J., Hubbard, M., Kelly, J., Kittridge, R., and Lucas, J., "Pencil Blister Reduction at Inland Steel Company," *Steelmaking Conference Proceedings*, Iron and Steel Society, Chicago, IL, USA, pp. 381–388, (1994)

[5] Thomas, B. G., "Modeling of continuous casting defects related to mold fluid flow," *Iron Steel Technol.*, 3(7), p. 127, (2006)

[6] Jin, K., Thomas, B. G., Liu, R., Vanka, S. P., and Ruan, X. M., "Simulation and validation of two-phase turbulent flow and particle transport in continuous casting of steel slabs," *IOP Conf. Ser. Mater. Sci. Eng.*, 84(1), p. 12095, (2015)

[7] Jin, K., Thomas, B. G., and Ruan, X., "Modeling and Measurements of Multiphase Flow and Bubble Entrapment in Steel Continuous Casting," *Metall. Mater. Trans. B*, 47(1), pp. 548–565, (2016)

[8] Zhang, L., Aoki, J., and Thomas, B. G., "Inclusion removal by bubble flotation in a continuous casting mold," *Metall. Mater. Trans. B*, 37(3), pp. 361–379, (2006)

[9] Yang, H. L., He, P., and Zhai, Y. C., "Removal Behavior of Inclusions in Molten Steel by Bubble Wake Flow Based on Water Model Experiment," *ISIJ Int.*, 54(3), pp. 578–581.

[10] Thomas, B. G., and Huang, X., 1993, "Effect of argon gas on fluid flow in a continuous slab casting mold," *76 th Steelmaking Conference*, pp. 273–289, (2014)

[11] Thomas, B. G., Huang, X., and Sussman, R. C., "Simulation of argon gas flow effects in a continuous slab caster," *Metall. Mater. Trans. B*, 25(4), pp. 527–547, (1994)

[12] Pfeiler, C., Wu, M., and Ludwig, A., "Influence of argon gas bubbles and non-metallic inclusions on the flow behavior in steel continuous casting," *Mater. Sci. Eng. A*, 413, pp. 115–120, (2005)

[13] Wang, Y., and Zhang, L., "Fluid Flow-Related Transport Phenomena in Steel Slab Continuous Casting Strands under Electromagnetic Brake," *Metall. Mater. Trans. B*, 42(6), pp. 1319–1351, (2011)

[14] Yuan, Q., Thomas, B. G., and Vanka, S. P., "Study of transient flow and particle transport in continuous steel caster molds: Part II. Particle transport," *Metall. Mater. Trans. B*, 35(4), pp. 703–714, (2004)

[15] Yuan, Q., 2004, *Transient study of turbulent flow and particle transport during continuous casting of steel slabs*, PhD Thesis, University of Illinois at Urbana-Champaign.

[16] Mahmood, S., *Modeling of Flow Asymmetries and Particle Entrapment in Nozzle and Mold During Continuous Casting of Steel Slabs*, MS Thesis, University of Illinois at Urbana-Champaign, (2006)

[17] Zhang, L., and Wang, Y., "Modeling the Entrapment of Nonmetallic Inclusions in Steel Continuous-Casting Billets," *JOM*, 64(9), pp. 1063–1074, (2012)

[18] Thomas, B. G., Yuan, Q., Mahmood, S., Liu, R., and Chaudhary, R., "Transport and entrapment of particles in steel continuous casting," *Metall. Mater. Trans. B*, 45(1), pp. 22–35, (2014)

[19] Singh, V., Dash, S. K., Sunitha, J. S., Ajmani, S. K., and Das, A. K., "Experimental simulation and mathematical modeling of air bubble movement in slab caster mold," *ISIJ Int.*, 46(2), pp. 210–218, (2006)

[20] Li, B., Okane, T., and Umeda, T., "Modeling of molten metal flow in a continuous casting process considering the effects of argon gas injection and static magnetic-field application," *Metall. Mater. Trans. B*, 31(6), pp. 1491–1503, (2000)

[21] Sanchez-Perez, R., García-Demedices, L., Ramos, J. P., Diaz-Cruz, M., and Morales, R. D., "Dynamics of coupled and uncoupled two-phase flows in a slab mold," *Metall. Mater. Trans. B*, 35(1), pp. 85–99, (2004)

[22] Liu, Z., Qi, F., Li, B., and Jiang, M., "Multiple Size Group Modeling of Polydispersed Bubbly Flow in the Mold: An Analysis of Turbulence and Interfacial Force Models," *Metall. Mater. Trans. B*, 46(2), pp. 933–952, (2015)

[23] Sussman, R. C., Burns, M. T., Huang, X., and Thomas, B. G., "Inclusion particle behavior in a continuous slab casting mold," *10th Process Technology Conference Proceedings.*, Iron and Steel Society, Toronto, Ontario, pp. 291–304, (1992)

[24] Yuan, Q., and Thomas, B. G., "Transport and entrapment of particles in continuous casting of steel," *Third Int. Congress on Science and Technology of Steelmaking*, pp. 745–762, (2005)

[25] Pfeiler, C., Thomas, B. G., Wu, M., Ludwig, A., and Kharicha, A., "Solidification and particle entrapment during continuous casting of steel," *Steel Res Int*, 79(8), pp. 599–607, (2008)

[26] Liu, Z., Li, B., Jiang, M., and Tsukihashi, F., "Modeling of transient two-phase flow in a continuous casting mold using Euler-Euler Large Eddy Simulation Scheme," *ISIJ Int.*, 53(3), pp. 484–492, (2013)

[27] Liu, C., Luo, Z., Zhang, T., Shen, D., Nan, W., and Zou, Z., "Mathematical Modeling of Multi-Sized Argon Gas Bubbles Motion and Its Impact on Melt Flow in Continuous Casting Mold of Steel," *J. Iron Steel Res. Int.*, 21(4), pp. 403–407, (2014)

[28] Thomas, B. G., Denissov, A., and Bai, H., "Behavior of argon bubbles during continuous casting of steel," *Steelmaking Conference Proceedings*, IRON AND STEEL SOCIETY OF AIME, pp. 375–384, (1997)

[29] Bai, H., and Thomas, B. G., "Bubble formation during horizontal gas injection into downward-flowing liquid," *Metall. Mater. Trans. B*, 32(6), pp. 1143–1159, (2001)

[30] Krepper, E., Lucas, D., Frank, T., Prasser, H.-M., and Zwart, P. J., "The inhomogeneous MUSIG model for the simulation of polydispersed flows," *Nucl. Eng. Des.*, 238(7), pp. 1690–1702, (2008)

[31] Liu, Z. Q., Qi, F. S., Li, B. K., and Cheung, S. C. P., "Modeling of bubble behaviors and size distribution in a slab continuous casting mold," *Int. J. Multiph. Flow*, 79, pp. 190–201, (2016)

[32] Sussman, R. C., Burns, M. T., Huang, X., and Thomas, B. G., "Inclusion particle behavior in a continuous slab casting mold," *Iron Steelmak.*, 20(2), pp. 14–16, (1993)

[33] Liu, Z., Li, B., and Jiang, M., "Transient Asymmetric Flow and Bubble Transport Inside a Slab Continuous-Casting Mold," *Metall. Mater. Trans. B*, 45(2), pp. 675–697, (2014)

[34] Yuan, Q., Thomas, B. G., and Vanka, S. P., "Turbulent flow and particle motion in continuous slab-casting molds," *Proc. Process Technol. ISSTech*, pp. 913–927, (2003)

[35] Liu, R., *Modeling transient multiphase flow and mold top surface behavior in steel continuous casting*, PhD Thesis, University of Illinois at Urbana-Champaign, (2015)

[36] Kobayashi, H., "The subgrid-scale models based on coherent structures for rotating homogeneous turbulence and turbulent channel flow," *Phys. Fluids*, 17(4), p. 45104, (2005)
[37] Kobayashi, H., "Large eddy simulation of magnetohydrodynamic turbulent duct flows," *Phys. Fluids*, 20(1), p. 15102, (2008)
[38] Singh, R., Thomas, B. G., and Vanka, S. P., "Effects of a magnetic field on turbulent flow in the mold region of a steel caster," *Metall. Mater. Trans. B*, 44(5), pp. 1201–1221, (2013)
[39] Singh, R., Thomas, B. G., and Vanka, S. P., "Large eddy simulations of double-ruler electromagnetic field effect on transient flow during continuous casting," *Metall. Mater. Trans. B*, 45(3), pp. 1098–1115, (2014)
[40] Rossin, P., and Rammler, E., "The laws governing the fineness of powdered coal," *J Inst Fuel*, 7, pp. 29–36, (1933)
[41] Liu, R., Cho, S.-M., Thomas, B. G., and Kim, S.-H., "Gas Flow Through Upper Tundish Nozzle Refractory and Bubble Size Evolution Inside SEN.", *CCC 2015 Conference*, (2015)
[42] Kuo, J. T., and Wallis, G. B., "Flow of bubbles through nozzles," *Int. J. Multiph. Flow*, 14(5), pp. 547–564, (1988)
[43] Crowe, C. T., Schwarzkopf, J. D., Sommerfeld, M., and Tsuji, Y., *Multiphase flows with droplets and particles*, CRC press, (2011)
[44] Legendre, D., and Magnaudet, J., "The lift force on a spherical bubble in a viscous linear shear flow," *J. Fluid Mech.*, 368, pp. 81–126, (1998)
[45] Yoshizawa, A., "A statistically-derived subgrid model for the large-eddy simulation of turbulence," *Phys. Fluids* 1958-1988, 25(9), pp. 1532–1538, (1982)
[46] Vanka, S. P., "2012 Freeman Scholar Lecture: Computational Fluid Dynamics on Graphics Processing Units," *J. Fluids Eng.*, 135(6), p. 61401, 2013
[47] Shinn, A. F., *Large eddy simulations of turbulent flows on graphics processing units: application to film-cooling flow*s, PhD Thesis, University of Illinois at Urbana-Champaign, (2011)
[48] Chaudhary, R., *Studies of Turbulent Flows in Continuous Casting of Steel With and Without Magnetic Field*, PhD Thesis, University of Illinois at Urbana-Champaign, 2011
[49] Kumar, P., Jin, K., and Vanka, S. P., "A Multi-GPU Based Accurate Algorithm for Simulations of Gas-Liquid Flows," *Proceedings of the 1st Thermal and Fluids Engineering Summer Conference*, American Society of Thermal and Fluids Engineers, New York City, pp. 1–17, (2016)
[50] Jin, K., Vanka, S. P., and Thomas, B. G., "Three-dimensional Flow in a Driven Cavity Subjected to an External Magnetic Field," *J. Fluids Eng.*, 137(7), p. 71104, (2015)
[51] Jin, K., Kumar, P., Vanka, S. P., and Thomas, B. G., "Rise of an argon bubble in liquid steel in the presence of a transverse magnetic field," *Phys. Fluids* 1994-Present, 28(9), p. 93301, (2016)
[52] Chaudhary, R., Thomas, B. G., and Vanka, S. P., "Effect of electromagnetic ruler braking (EMBr) on transient turbulent flow in continuous slab casting using large eddy simulations," *Metall. Mater. Trans. B*, 43(3), pp. 532–553, (2012)